

BOP-Distrib: Revisiting 6D Pose Estimation Benchmarks for Better Evaluation under Visual Ambiguities

Boris Meden¹ Asma Brazi^{1,2} Fabrice Mayran de Chamisso¹ Steve Bourgeois¹
¹Université Paris-Saclay, CEA, List ²LIGM, Ecole des Ponts

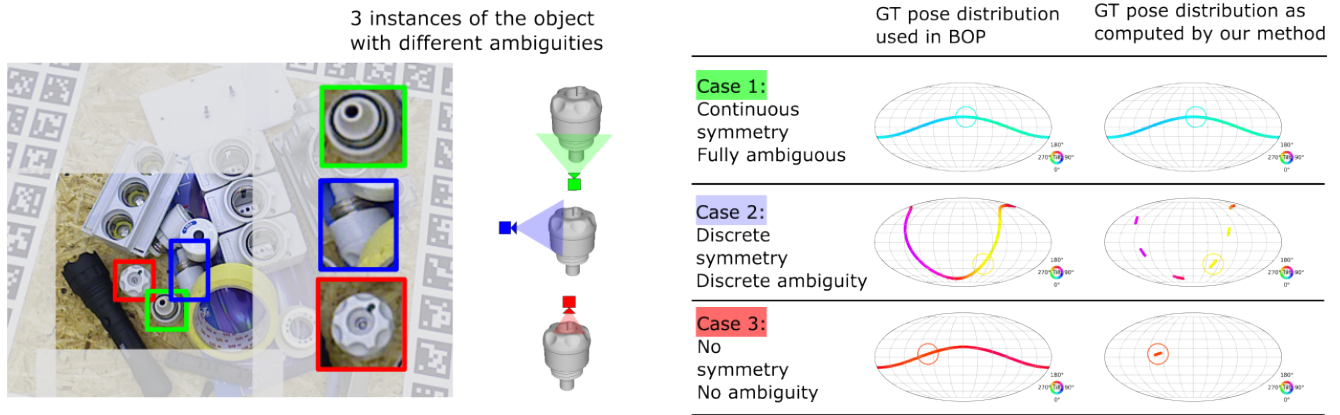


Figure 1. We provide for the first time 6D pose annotations in the form of a per-image object pose distribution. Current annotations in BOP [17] datasets are given as a single pose, shown here as a circle in the $SO(3)$ representations. T-LESS [13] also provides a symmetry pattern leaving the 3D object model invariant, from which a distribution can be computed (the colored points in the $SO(3)$ representations). Such distribution however does not cover many cases [29]: For the object in this example, when only its core is visible (**Case 1**), the pose is fully ambiguous and should be represented by a continuous distribution in $SO(3)$. When the sides of the head are visible (**Case 2**), there are still ambiguities and the distribution is made of 6 modes. When the hole is visible (**Case 3**), there are no ambiguities, and the pose distribution should be concentrated around one pose. Our method annotates the T-LESS dataset with *per-image* distributions, taking into account the partial occlusions and allowing us to evaluate a predicted pose properly. We show that considering these distributions for evaluating state-of-the-art methods results in a significant change of ranking for the BOP challenge. Such ground truth distributions also become a key asset when it comes to evaluating pose distribution estimation methods [9, 19]. With appropriate metrics, we demonstrate the first quantitative evaluation of pose distribution methods on real images, as an extension to single pose methods.

Abstract

6D pose estimation aims at determining the pose of the object that best explains the camera observation. The unique solution for a non-symmetrical object can turn into a multi-modal pose distribution for a symmetrical object or when occlusions of symmetry-breaking elements happen, depending on the viewpoint. Currently, 6D pose estimation methods are benchmarked on datasets that consider, for their ground truth annotations, visual ambiguities as only related to global object symmetries, whereas they should be defined per-image to account for the camera viewpoint. We thus first propose an automatic method to re-annotate those

datasets with a 6D pose distribution specific to each image, taking into account the visibility of the object surface in the image to correctly determine the visual ambiguities. Second, given this improved ground truth, we re-evaluate the state-of-the-art single pose methods and show that this greatly modifies the ranking of these methods. Third, as some recent works focus on estimating the complete set of solutions, we derive a precision/recall formulation to evaluate them against our image-wise distribution ground truth, making it the first benchmark for pose distribution methods on real images. We will make our annotations for the

1. Introduction

Visual 6D pose estimation of an object consists in determining the 3D position and orientation of this object with respect to the camera that explains the observed image. It is a key task in many application domains, such as robotics (e.g. grasping or manipulation), augmented reality, industrial quality control, etc. In such contexts, datasets of images with ground-truth poses are of primary importance, since they can be used to train learning based methods, but first and foremost to benchmark the performances of proposed approaches. The annotation accuracy of reference benchmarks, such as BOP [42] for 6D pose estimation, is thus crucial since it influences the research directions.

However, annotating images of objects with their 6D poses is a complex task. This is especially true when considered objects include symmetrical parts. Indeed, as illustrated in Figure 1, an image does not necessarily correspond to a single pose solution depending on the viewpoint and occlusions. While symmetrical objects naturally imply multiple solutions, non-symmetrical objects can also yield multiple solutions in case of partial occlusions. Current reference benchmarks [42] ignore these occlusion-induced symmetries, resulting in an imperfect evaluation of the methods. As we will show, considering better ground truth distributions results in a significant change of ranking of current pose estimation methods.

In this paper, we first propose a method that automatically annotates pose distributions for images that take into account the ambiguities due to the object symmetries but also to the partial occlusions. Our method exploits the current annotations as a starting point, the ground truth visibility masks of the objects, and their 3D models. While we demonstrate it on T-LESS [13], our method is fully automatic and can be applied to other datasets as demonstrated on YCB-V [47].

We also re-evaluate classical metrics with these annotations to assess the performance of pose estimation methods that return a single pose estimate per image. This yields a strongly modified ranking of current challenger methods.

Moreover, we also consider the few methods that already predict multi-modal pose distributions [9, 19]. Because of the absence of proper annotations, these methods have been evaluated quantitatively only on synthetic images and only qualitatively on real images. Thanks to our annotations, we are able to provide their first evaluation on real data.

In summary, our contributions are the following:

1. A novel automatic method computing a multi-modal 6D pose distribution ground truth from a unique ground truth pose and a proposal set of object symmetries;

2. A comprehensive re-evaluation of 6-DOF single pose estimation methods related to the re-annotation of the T-LESS [13] ground-truth;
3. A new evaluation framework of 6-DOF pose distribution estimation methods, which makes it the first multi-modal pose distribution benchmarking on real data.

Our annotations and code will be made public.

2. Related Work

Object 6D pose estimation aims at determining an object pose that best explains the camera observation. While the solution is unique when the object is non-symmetrical and not occluded, multiple equivalent possible solutions arise when the object is symmetrical or when the occlusions prevent the observation of symmetry-breaking elements.

While the state of the art mostly focused on estimating a single pose [6, 8, 15, 23, 38, 40, 41, 44], some recent works focus on estimating the complete set of solutions [9, 18, 19, 22, 29, 30, 33, 36]. As we argue below, to properly evaluate the performance of a method, ground truth annotations including the complete set of solutions for each test image, and metrics that take into account the multiplicity of the solutions, are required, even for methods that return a single pose per image.

Datasets and 6D pose annotation. Various techniques have been introduced to annotate image datasets with their 6D poses. For synthetic datasets [2, 43], the ground truth pose is directly available, while, for real datasets, this pose is usually determined with the help of user interaction [5, 7, 14], markers [1, 10, 11], or a robotic arm [31, 45], and refined with ICP in the case of an RGB-D camera [7, 14, 31, 45].

However, such annotations only provide a single pose solution while multiple may exist. For fully symmetric objects, the solutions are always related with the same set of rigid transforms, independently of the viewpoint or the occlusions. This set of transforms, also called *symmetries pattern*, can then be pre-computed offline and applied to the initial solution to recover the whole set of solutions [16].

For non-symmetrical objects, recovering the complete set of solutions is much more challenging since symmetries may arise from the non-visibility of disambiguating parts of the object, those non-visibilitys being induced by the viewpoint (self-occlusion), by other elements of the scene (external occlusion). The transformation set that relates the different solutions is then specific to each image and cannot be pre-computed from the 3D object model.

To our knowledge, no method has been proposed to determine this ground-truth transformation set per image. Instead, the current gold standard in 6D pose estimation benchmarks still consists in approximating this per-image

transformation set with a unique global transformation set. The latter is usually computed with the same method than fully symmetric object with large enough tolerance to ignore small disambiguating elements (*e.g.* surface deviation tolerance of 1.5cm or 10% of the object diameter [16]).

Evaluation metrics. Performance evaluation usually differs depending on whether the method is used to output a single pose or a distribution.

For single pose estimation, the accuracy is measured through the deviation of the object surface points when transformed by the estimate and by the ground truth pose (registration error) [12]. Depending on the sensor used—RGB or RGB-D—and the targeted application (*e.g.* robotics or Augmented Reality), deviations can be measured in 3D space (3D distance) or in the image space (re-projection error), and the registration error can be considered as the mean or maximal error over the object surface. In case of multi-valued ground-truths due to a symmetrical object or occlusion-induced symmetries, the accuracy corresponds to the minimal error with respect to the set of solutions [12, 43, 47]. In practice, the most commonly used accuracy measures are :

1. Average Distance metric (ADD), and variations for symmetrical objects (ADD-S [47], ADD-H [43]), target to measure mean Euclidean error between surface points of the object transformed with the estimated pose and the ground truth pose, but are replaced by MSSD now.
2. Visual Surface Discrepancy (VSD) [14] measures misalignment over the visible surface of the object model. VSD is more expensive to compute than MSSD and MSPD, and requires a depth image. It is now omitted for new tasks as stated by BOP organizers¹.
3. Maximum Symmetry-Aware Surface Distance (MSSD) [16] which is similar to ADD but considers the maximal error instead of the mean error and symmetry management. MSSD provides a 3D error, useful to robotics applications.
4. Maximum Symmetry-Aware Projection Distance (MSPD) [16] measures the maximum reprojection error between the projection of the visible points with the ground-truth pose and their corresponding projection with the pose to evaluate and symmetry management. MSPD provides a reprojection error, useful to augmented reality applications.

Based on these accuracy measures, and inspired from the evaluation of the detection methods, single 6D pose estimation methods are usually evaluated through Precision/Recall. In such evaluation frameworks, an estimated pose is considered as correct if its registration error is below a predefined threshold. The precision corresponds to the rate of correct pose estimations, meaning the ratio of

the estimated poses that are correct over the number of estimated poses. The recall corresponds to the rate of correctly registered objects, meaning the ratio between the number of object instances in the dataset whose pose was considered as correct over the number of object instances in the dataset.

Regarding the evaluation of multi-modal 6D pose distribution estimation methods, the accuracy is usually measured as a pose error, meaning the minimal deviation between the inferred rotation and translation and the corresponding nearest ground truth pose [9, 20, 33, 39].

If the method outputs a probability distribution over the whole pose space, the method is usually evaluated through its spread, corresponding to the expectation of the pose error and the log-likelihood between the inferred distribution and the multi-valued solution [9, 18, 20, 33, 39], meaning the sum of the mean log probability at ground truth solutions. While the spread provides a probabilistic measure of the accuracy, the log-likelihood measures how similar the probability distributions are. This penalizes the method if some ground truth solutions are missing in the estimate.

However, not all multi-modal 6D pose estimation methods actually provide a full probability distribution over the whole pose space. Instead, some methods output a set of poses corresponding to some local maxima of the underlying probability distribution [19]. For such methods, performances can be evaluated through the Precision/Recall of the multi-valued estimation. A pose estimate is then considered as correct with respect to one ground truth pose if its distance in pose space does not exceed a threshold δ . The Precision for a given image is then defined as the ratio of the number of estimated poses whose distance have at least one ground truth pose that does not exceed the threshold δ over the total number of estimated poses. The Recall for an object image is then defined as the ratio between the number of ground truth poses whose distance have at least one estimated pose that does not exceed the threshold δ over the total number of ground truth poses. Similarly to the spread and log likelihood, these precision and recall are related to the multi-modal pose distribution.

Our method combines a ground truth pose and a symmetries pattern to represent the pose distribution for each image. Unlike previous works, the symmetries pattern is adjusted to each image, taking into account its specific viewpoint and occluded objects (Section 3). Moreover, whereas single pose and multi-modal distribution pose methods are currently evaluated with non-comparable metrics, we introduce new evaluation metrics for multi-modal methods that are homogeneous with single pose methods (Section 4).

3. Method

As shown in Figure 2, the probability of a pose explaining a given image of the object is related to the visibility of the different points on the surface of the object.

¹<https://bop.felk.cvut.cz/challenges/>

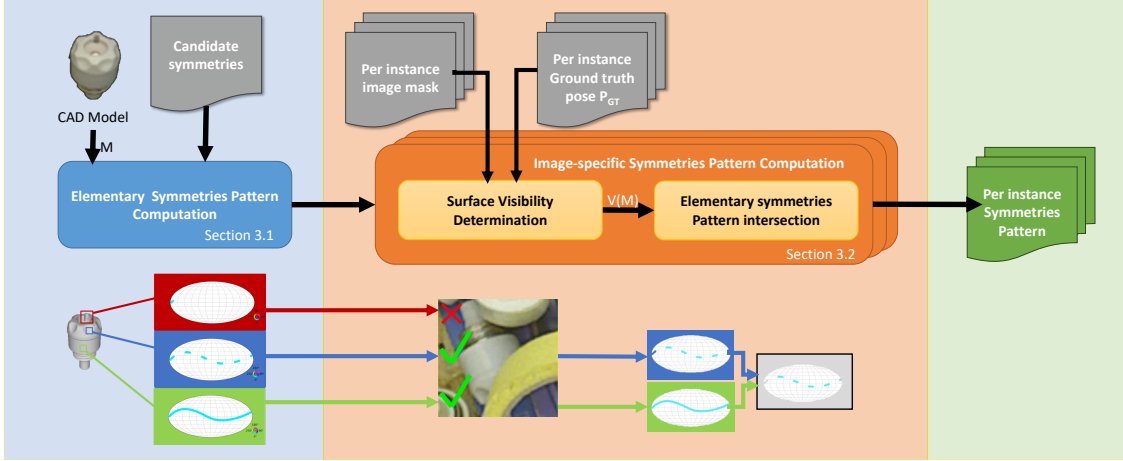


Figure 2. **Overview of our method.** From a symmetry candidate set, we pre-compute the object per-vertex ϵ -sym. Then for a given scene, we compute the vertices visibility and perform a robust intersection between their ϵ -sym. This intersection constitutes the symmetry pattern of this object instance in this scene. When multiplied by the ground truth, we obtain the SE(3) distribution of the object instance.

More formally, given an image I and a ground truth pose P_{GT} for a target object in this image, the objective of our method is to recover the set $\mathcal{T} = \{T_i \in SE(3)\}$ of rigid transformations that transform the ground truth pose P_{GT} into another pose that results in the same appearance of the object. In the following, we will call set \mathcal{T} the *symmetry pattern* of image I .

Depending on the geometry M of the object and the set $\mathcal{V}(M)$ of its visible points, set \mathcal{T} can be limited to the identity transform in the case of a non-ambiguous pose or can include multiple transformations in addition to the identity. As introduced in [12], \mathcal{T} can be defined as partial ϵ -symmetries of $\mathcal{V}(M)$:

$$\epsilon\text{-sym}(\mathcal{V}(M), M) = \{T_i : d(T_i * \mathcal{V}(M), M) < \epsilon\}, \quad (1)$$

where d measures the mean deviation between the points of $\mathcal{V}(M)$ and M , ϵ is the maximal surface deviation tolerance and $*$ represents the application of the transformation T_i onto the point cloud $\mathcal{V}(M)$.

If the set $\mathcal{V}(M)$ of visible points is available, the symmetry pattern could in principle be approximated by sampling the rigid transformation space SE(3) and assessing whether the sample belongs to the ϵ -symmetries. However, since sampling a 6D space becomes quickly computationally expensive, such annotation process was never used to our knowledge.

In the following sections, we introduce solutions to reduce the computational cost (Section 3.1), how to introduce some tolerance in the evaluation of the ϵ -symmetries (Section 3.2), and how to extend the annotation to textured objects (Section 3.3).

3.1. Speeding up the computation of ϵ -sym

Computing ϵ -symmetries for each instance of image of a dataset can quickly become time consuming since it implies to sample the 6D pose space around the ground truth pose. To accelerate the computation of the ϵ -symmetries, we reformulate them to introduce image-independent terms that can be pre-computed.

First, by definition of the ϵ -symmetries, for any subsets $V_1 \subset \mathcal{V}(M)$ and $V_2 \subset \mathcal{V}(M)$, we have:

$$\epsilon\text{-sym}(V_1 \cup V_2, M) = \epsilon\text{-sym}(V_1, M) \cap \epsilon\text{-sym}(V_2, M). \quad (2)$$

Therefore, we can reformulate Equation 1 as:

$$\epsilon\text{-sym}(\mathcal{V}(M), M) = \bigcap_{v_j \in \mathcal{V}(M)} \epsilon\text{-sym}(v_j, M), \quad (3)$$

where v_j is a 3D point and $\epsilon\text{-sym}(v_j, M)$ is the symmetry pattern when the point v_j is the only visible point, which we name *elementary symmetry pattern* of v_j .

With such expression of the ϵ -symmetries, it appears that elementary symmetry patterns can be pre-computed for the whole 3D object model M since they are independent of the image. Only the set of visible points and the intersection of the corresponding pre-computed elementary symmetries patterns need to be computed per image.

3.2. Robust symmetries patterns intersection

In practice, using a strict intersection might reject too many transformations since a transformation T_i would be kept only if it is part of all the elementary symmetries patterns. Instead, we prefer to use a soft intersection, meaning that the transformation T_i will be included even if a few patterns do not include T_i . This soft intersection is achieved

by counting, for each transformation T_i , the number of elementary symmetries patterns that include T_i . This counting is defined as follows, in the form of a histogram over \mathcal{T} :

$$\forall i, H(T_i) = \text{Card}\{v_j \mid v_j \in \mathcal{V}(M), T_i \in \epsilon\text{-sym}(v_j, M)\}. \quad (4)$$

A strict intersection would only keep the T_i with the maximum value of $H(T_i)$ which is represented by $H(Id)$ as the identity of $SE(3)$ and is always in the symmetry pattern. Our soft intersection tolerates a threshold and keeps all the T_i such that $H(T_i) > H(Id) - \tau$, where τ represents the minimum size (expressed in number of 3D points) of the symmetry-breaking elements.

3.3. Generalization to textured 3D objects

While the process previously described considered only texture-less 3D objects, the method can be extended to textured ones by simply redefining the ϵ -symmetries as:

$$\epsilon\text{-sym}(\mathcal{V}(M), M) = \{T_i : d(T_i * \mathcal{V}(M), M) < \epsilon, d_{\text{color}}(T_i * \mathcal{V}(M), M) < \zeta\}, \quad (5)$$

where d_{color} is the distance in color-space and ζ is the color deviation tolerance.

4. Evaluating 6D Pose Distribution Predictions

Currently, single pose estimation methods and distribution pose estimation methods are evaluated on different datasets (BOP challenge for single poses, SYMSOL for 6D pose distributions) with different metrics (registration error for single pose estimation, pose error for 6D pose distribution). With our annotation method that provides the full set of 6D pose solutions even on real data, it becomes possible to evaluate both tasks on the same dataset. However, it would be beneficial if both tasks can be evaluated with comparable metrics.

We therefore propose to keep the evaluation process of single pose method unchanged, but on a more accurate ground truth, and to extend it to pose distributions evaluation. First, whereas pose error is commonly used in 6D pose distribution evaluation process [9, 20, 33], we propose to use the registration error. The latter takes the object 3D shape into account, making the accuracy more meaningful for most of the applications. It is also the type of error used by the current gold standard benchmark for single pose [42]. Typically, we suggest to use the Maximal Surface Distance (MSD) and Maximum Projective Distance (MPD) metrics. Second, we propose to keep the metrics of Precision and Recall, but we adapt them to measure Precision over the whole estimated distribution of poses instead of a unique pose, and Recall over the whole set of solutions instead of considering a pose to be found if one of its multiple solutions was found.

Precision for pose distribution. We define the precision in the case of pose distribution prediction as:

$$\mathbf{P}_{\mathbf{d}}(\text{Est}, \text{GT}) = \sum_{P_{\text{Est}}^j \in \text{Est}} p(P_{\text{Est}}^j) \left(\min_{P_{\text{GT}} \in \text{GT}} d(P_{\text{Est}}^j, P_{\text{GT}}) < \tau_{\mathbf{d}} \right), \quad (6)$$

where Est and GT are respectively the estimated and the ground truth distributions to compare, and $p(\text{Est}_i)$ represents the probability associated to the i -th element of the estimated distribution², \mathbf{d} is the chosen registration distance, and $\tau_{\mathbf{d}}$ the associated threshold.

Recall for pose distribution. Similarly to the precision, we define the recall in the case of pose distribution prediction as:

$$\mathbf{R}_{\mathbf{d}}(\text{Est}, \text{GT}, \tau_{\mathbf{d}}) = \sum_{P_{\text{GT}}^i \in \text{GT}} \max \left(p(\hat{P}_{\text{Est}}^i), \frac{1}{\text{Card}(\text{GT})} \right) [d(\hat{P}_{\text{Est}}^i, P_{\text{GT}}^i) < \tau_{\mathbf{d}}],$$

with $\hat{P}_{\text{Est}}^i = \arg \min_{P_{\text{Est}} \in \text{Est}} d(P_{\text{Est}}, P_{\text{GT}}^i)$. (7)

The probability of \hat{P}_{Est}^i is clamped to $\frac{1}{\text{Card}(\text{GT})}$ since ground truth poses are considered as equiprobable.

5. Experiments

In this section, after evaluating the performances of our annotation method (Section 5.2), we present and discuss the impact of our ground-truth annotations and evaluation metrics onto the evaluation of state-of-the-art solutions for both single pose estimation (Section 5.3) and multi-modal pose distribution estimation (Section 5.4).

Since our annotation process and metrics are related to objects with intrinsic or occlusion-induced symmetries, we perform our evaluations on the T-LESS dataset. Indeed, among the datasets of the BOP challenge [17], T-LESS appears to be the only dataset to exhibit symmetrical objects, with occlusion-induced symmetries, real data and public ground-truth annotations: ITODD [7] and Homebrewed [21] feature symmetrical objects, with occlusion-induced symmetries, but do not publicly share their ground-truths. HOPE [43] and IC-BIN [5] have symmetrical shapes, but texture information disambiguates them completely.

The first experiment focus on a qualitative evaluation of our annotation method (Section 5.2). The second evaluates the impact of our re-annotation of T-LESS Dataset on the performance evaluation of the best performer methods of

²If the method outputs solutions without assigning a probability to each pose, such as [19], a uniform probability over the solutions is used.

the BOP benchmark [17] on single pose estimation (the Multiple instances of Multiple known objects (MiMo) task of BOP) (Section 5.3). The last experiment evaluates for the first time methods of 6D pose distribution estimation on a non-synthetic dataset with proper annotations and metrics (Section 5.4).

5.1. Implementation details

In our experiments, we sample surface points from the CAD models with a resolutions of 0.5mm. For the pre-computation of elementary symmetries patterns for a given object, we use the per-object symmetries pattern given by the BOP challenge [17] as the initial symmetry candidates, with a tolerance factor ϵ -sym set to 1mm.

The object surface visibility $\mathcal{V}(M)$ is computed by Z-buffering using ground truth pose P_{GT} and the 3D model of the object. For the robust symmetry pattern intersection, the soft intersection tolerance factor τ was experimentally adjusted to 28 3D points, resulting in a minimal disambiguating element size of roughly $2.5 \times 2.5 \text{mm}^2$.

5.2. Qualitative validation of the method

We illustrate qualitatively the results obtained on some images of the T-LESS dataset in Figure 3. We can observe the coherence between the distribution and the visibility of the disambiguating elements. Since this dataset does not contain any image with visual ambiguity for the translational part of the pose, the ground truth translation is always reduced to a single 3D point. More visualizations are provided in the supplementary material to convince the reader of the quality of our annotations.

5.3. Single Pose Estimation Evaluation

Since May 2023, raw results of BOP Challenge [17] public submissions have become publicly available to allow in-depth analysis. In this experiment, we use them to compare the performance evaluations of state-of-the-art methods on T-LESS for both the original 6D annotations and our annotations. We considered top contenders of the BOP challenge for the pose estimation and pose estimation for unseen objects tasks. We also included two methods for the multi-modal pose distribution estimation task [9, 19] for which we kept only the mode with highest confidence. We consider their full predicted distributions in the next subsection. Since these methods are not part of the BOP challenge, we retrained them on the T-LESS train set.

Experimental protocol. We evaluate the current (July 2024) top contenders of the BOP Challenge on the T-LESS dataset [13] on the **pose estimation** task and the **pose estimation of unseen object** task together with [9, 19]. We conduct a similar evaluation with YCB-V [47].

This evaluation is based directly on the raw pose results provided by the contenders and the official evaluation scripts of BOP challenges, both being publicly available on the Challenge website. Following the BOP Challenge, the evaluation is based exclusively on recall. Our method ranking is based on the mean of Recalls computed on MSPD and MSSD accuracies.

Results. Table 1 reports the results. We can observe a large impact of the ground truth on the methods results (see **Loss** column) and ranking. In terms of ranking, the well established **pose estimation** task face the biggest changes, with `gdrnppdet-pbrrealmegapose-multihyp` moving from the 12th to the 3rd position for RGB methods and `surfemb-pbr-rgb-lin` [8] moving from the 16th to the 5th place for the RGB-D methods. For **pose estimation of unseen objects**, the difference of ranking can reach 6 places.

We observe large impacts on the recall performances as well. Whereas 29 of the 30 contenders of **pose estimation** task have a mean recall up to 80% and even up to 90% for 6 methods with the original annotations, only 4 methods exceed this score with our annotations, with a majority of methods having less than 65%. Similarly, most of the contenders for the **pose estimation of unseen objects** task have a mean recall that exceeds 50% with the original annotations whereas only the 2 best RGB-D methods exceed this score once evaluated with our annotations. As shown in Figure 1 (**Case 3**), the image-wise annotation rejects poses when the image is not ambiguous. The Loss is explained by inaccurate pose estimates that were mistakenly validated by previous object-wise annotations (see supplementary material for visualizations).

It is also interesting to note that the ranking order of variants **v1.2**, **v1.3** and **v1.4** of GDRNPP RGB-D (based on different object detectors, training augmentations, and refinement methods) is changed when evaluated with our ground truth. It underlines that inaccurate ground truth annotation can induce erroneous conclusions in ablation studies.

5.4. Pose Distribution Evaluation

We provide now the first evaluation of 6D pose distribution estimation methods on a dataset of real images.

Experimental protocol Similarly to Section 5.3, the methods were trained on the train set of T-LESS. The ground truth used for this dataset is the same than the one of Section 5.3 and is constituted of a discrete set of 6D pose obtained with the 6D pose annotation process introduced in Section 3. The performances of the methods are evaluated in Precision and Recall, using accuracy measures MPD and MSD as introduced in Section 4. More details on methods processing and results formatting are given in the supplementary material.

		BOP [42] (object-wise annotations)				BOP-Distrib (our image-wise annotations)				
BOP Contenders		MSSD	MSPD	Mean	Rank	MSSD	MSPD	Mean	Loss	Rank
T-LESS [13] BOP Challenge 2023 [17]: pose estimation of unseen objects										
RGB	foundpose [37]	55.0	62.3	58.6	1	45.5	52.1	48.8	-9.8	3(-2)
	gigaposemegapose-5-hypothesis [24, 35]	54.3	62.0	58.1	2	45.3	52.3	48.8	-9.3	2
	gigaposemegapose-1-hypothesis [24, 35]	51.5	59.2	55.3	3	38.5	45.1	41.8	-13.5	9(-6)
	genflow-multihypo16-rgb [32]	50.9	57.9	54.4	4	45.9	52.4	49.1	-5.3	1(↑3)
	genflow-multihypo-rgb [32]	50.4	57.3	53.9	5	44.9	51.4	48.1	-5.8	4(↑1)
	genflow-multihypo16 [32]	52.8	54.8	53.8	6	46.7	48.6	47.7	-6.1	5(↑1)
	genflow-multihypo [32]	51.6	53.6	52.6	7	45.2	47.2	46.2	-6.4	6(↑1)
	foundpose [37]	49.1	55.6	52.4	8	37.7	43.4	40.6	-11.8	11(-3)
	foundpose [37]	49.1	55.6	52.3	9	37.7	43.4	40.5	-11.8	12(-3)
	cnos-fastsammegapose-multihyp-10 [24, 34]	48.5	55.9	52.2	10	40.6	47.1	43.8	-8.4	7(↑3)
	cnos-fastsammegapose-multihyp [24, 34]	48.4	55.6	52.0	11	40.5	47.1	43.8	-8.2	8(↑3)
	cnos-fastsammegapose-multihyp-teaserpp [24, 34]	48.4	51.3	49.9	12	40.3	43.0	41.7	-8.2	10(↑2)
RGB-D	foundationpose [46]	62.9	64.1	63.5	1	56.7	58.0	57.4	-6.1	1
	gigaposegenflowkabsch [35]	56.3	58.6	57.5	2	49.4	51.7	50.6	-6.9	2
	sam6d [26]	52.9	54.5	53.7	3	39.7	41.2	40.4	-13.3	3
	sam6d [26]	52.1	53.5	52.8	4	38.3	39.7	39.0	-13.8	5(-1)
	sam6d-fastsam [26]	49.9	51.1	50.5	5	37.9	39.1	38.5	-12.0	6(-1)
	sam6d-cnsmask [26]	50.0	50.9	50.4	6	39.3	40.3	39.8	-10.6	4(↑2)
	sam6d-cnsmask [26]	49.3	50.5	49.9	7	37.2	38.4	37.8	-12.1	7
	sam6d-zeropose [26]	44.4	45.6	45.0	8	33.5	34.8	34.2	-10.8	8
	zeropose-multi-hypo-refinement-defaultseg [4]	41.5	42.0	41.8	9	29.4	30.1	29.7	-12.1	9
	T-LESS [13] BOP Challenge 2022 [42]: pose estimation									
RGB	hccepose-2024-pbr	82.9	95.8	89.4	1	53.8	65.2	59.5	-29.9	5(-4)
	hcceposeefficientnet-b4-default-2d-bbox	81.4	94.8	88.1	2	53.1	64.5	58.8	-29.3	6(-4)
	cosypose-eccv20-syntreal-8views [23]	83.6	90.7	87.2	3	57.2	64.0	60.6	-26.6	4(-1)
	hccepose-default-2d-bbox	79.2	93.2	86.2	4	51.4	63.1	57.2	-29.0	8(-4)
	gdmppdet-pbrrealgenflow-multihypo-rgb [28, 44]	78.4	92.2	85.3	5	69.9	82.9	76.4	-8.9	2(↑3)
	leroy-fuseocclu-rgb	78.0	91.7	84.8	6	70.4	83.3	76.9	-7.9	1(↑5)
	gpose2023-rgb [48]	76.6	92.9	84.7	7	50.2	64.0	57.1	-27.6	9(-2)
	gdmpp-pbr-rgb-mmodel [28, 44]	76.3	92.4	84.4	8	50.0	63.6	56.8	-27.6	10(-2)
	gdmpp-pbrreal-rgb-mmodel [28, 44]	76.0	91.3	83.6	9	48.8	61.7	55.2	-28.4	13(-4)
	cosypose-eccv20-syntreal-4views [23]	79.5	86.4	83.0	10	52.7	59.3	56.0	-27.0	12(-2)
	mrc-net [25]	78.5	87.1	82.8	11	52.3	60.3	56.3	-26.5	11
	gdmppdet-pbrrealmegapose-multihyp [28, 44]	74.0	87.4	80.7	12	61.6	73.8	67.7	-13.0	3(↑9)
	sc6d [3]	72.1	85.3	78.7	13	52.6	64.1	58.3	-20.4	7(↑6)
RGB-D	gpose2023 [48]	92.1	94.6	93.4	1	86.5	89.1	87.8	-5.6	1
	gdmppv2-rgb-d-pbrreal [28, 44]	90.2	92.6	91.4	2	84.8	87.2	86.0	-5.4	3(-1)
	gpose2023-pbr [48]	90.3	92.6	91.4	3	84.7	87.2	86.0	-5.4	2(↑1)
	modalocclusion-rgb-d	89.7	92.9	91.3	4	83.2	86.4	84.8	-6.5	4
	hcceposebf-2024-ref	89.0	91.7	90.3	5	71.7	74.7	73.2	-17.1	6(-1)
	gdrbpb-pbrreal-rgb-d-mmodel-fast v1.4 [28, 44]	88.7	91.5	90.1	6	58.1	61.9	60.0	-30.1	13(-7)
	gdmpp-pbrreal-rgb-d-mmodel v1.3 [28, 44]	88.4	90.9	89.6	7	60.6	63.7	62.2	-27.4	10(-3)
	gdmpp-pbrreal-rgb-d-mmodel v1.2 [28, 44]	87.1	90.3	88.7	8	57.5	61.2	59.3	-29.4	15(-7)
	zebrasoset-effnetb4-refineddefdet-2023 [40]	87.3	90.2	88.7	9	60.2	63.4	61.8	-26.9	11(-2)
	gdmpp-pbr-rgb-d-mmodel v1.1 [28, 44]	87.2	90.1	88.7	10	60.8	64.2	62.5	-26.2	9(↑1)
	hipose-cvpr24 [27]	86.6	88.8	87.7	11	58.0	60.8	59.4	-28.3	14(-3)
	defaultdetection-pfa-mixpbr-rgb-d	85.5	87.7	86.6	12	59.2	62.0	60.6	-26.0	12
	zebrasoset-effnetb4defdet-2023 [40]	79.1	93.0	86.1	13	51.8	63.4	57.6	-28.5	17(-4)
	zebrasoset-effnetb4pbr-only-defdet-2023	77.7	92.0	84.9	14	50.7	62.8	56.8	-28.1	18(-4)
	gdmpp-pbrreal-rgb-d-mmodel-officialdet v1.0 [28, 44]	83.4	85.6	84.5	15	57.5	60.2	58.9	-25.6	16(-1)
	surfemb-pbr-rgb-d-lin [8]	82.9	85.9	84.4	16	75.8	78.7	77.2	-7.2	5(↑11)
	poseio	81.7	86.0	83.8	17	69.3	73.6	71.4	-12.4	8(↑9)
YCB-V [47] BOP Challenge 2022 [42]: pose estimation										
RGB	cosypose-eccv20-syntreal-8views [23]	88.5	88.0	88.2	1	83.3	82.4	82.9	-5.3	2(-1)
	cosypose-eccv20-syntreal-4views [23]	86.9	86.6	86.8	2	82.1	81.3	81.7	-5.1	4(-2)
	mrpe-pbrreal-rgb-smodel	85.7	87.3	86.5	3	83.1	84.4	83.7	-2.8	1(↑2)
	magic	85.9	85.4	85.6	4	82.9	82.3	82.6	-3.0	3(↑1)
RGB-D	gdmppv2-rgb-d-pbrreal [28, 44]	96.3	92.7	94.5	1	94.2	90.2	92.2	-2.3	1
	gpose2023 [48]	96.2	92.6	94.4	2	94.2	90.2	92.2	-2.2	2
	gdmpp-pbrreal-rgb-d-mmodel [28, 44]	95.7	91.9	93.8	3	90.1	86.2	88.1	-5.7	3
	dsgc6d	93.0	90.1	91.5	4	87.5	85.2	86.4	-5.1	4
T-LESS [13] Best mode of pose distribution methods										
RGB	LiePose Diffusion [19]	60.1	92.2	76.1	1	48.3	76.1	62.2	-13.9	2(-1)
	SpyroPose [9]	61.2	75.3	68.3	2	57.8	71.6	64.7	-3.6	1(↑1)

Table 1. **Results of BOP 2023 on T-LESS [13] and YCB-V [47] with our annotations.** We report the top contenders results of the **pose estimation of unseen objects challenge** and the **pose estimation challenge** evaluated with MSSD and MSPD on both the official ground truth (object-wise) and our ground truth (image-wise). We rank the methods with the mean of MSSD and MSPD (similar to BOP, except we exclude VSD as BOP starts to abandon it) and re-rank them with the mean of MSSD and MSPD computed on our ground truth distributions. The drop in the scores highlighted by the **Loss** column ($\text{Loss} = \text{Mean}_{\text{BOP-Distrib}} - \text{Mean}_{\text{BOP}}$) produces drastic changes in the rankings. We also show the same scores for the **best mode of distribution estimation methods**, however, both of them use ground truth bounding boxes instead of a detector, so direct comparison would be unfair. This highlights the importance to consider image level symmetries as we proposed, to evaluate accurately pose estimation methods. We also processed YCB-V. The **Loss** is much lower as there are fewer symmetrical objects. Names of the methods are automatically processed from BOP csv result files.

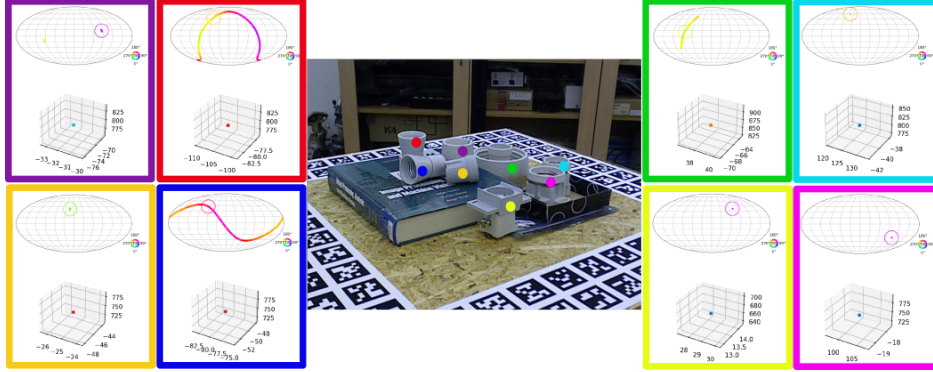


Figure 3. **Visualizations of our ground truth.** We display SE(3) ground truth distributions for scene 16 of T-LESS [13]. Circle on orientation diagram represents the unique ground truth pose provided as input to our method. Colors are used to link object instances to their distributions. More visualizations are provided in the supplementary material to convince the reader of the quality of our annotations.

Results We evaluated SpyroPose [9] and LiePose-Diffusion [19] (either PBR + real images and PBR only to compare with SpyroPose) since they provide 6D pose distributions, unlike [18, 33] that provide distributions only over the rotation. To show genericity, we also evaluated the top 3 RGB methods of single **pose estimation** task (with image-wise annotations). Their distribution is considered as a Dirac distribution on the single estimate. Results are given on the complete dataset, and the subset of objects with cylindrical symmetry (1-4, 13-18, 24 and 30, as illustrated in supplementary material).

Quantitative results are reported on Table 2 whereas qualitative results are provided in the supplementary material. It appears that LiePose-Diffusion outperforms SpyroPose, except for the Precision MSD. Lower accuracy are obtained with MSD error since those methods use RGB images only and no depth. Single pose methods outperform distribution methods in terms of Precision, as they are optimized for that. Yet, distribution methods produce much stronger Recalls, even more on only symmetrical objects, highlighting their ability to retrieve multiple meaningful poses from the targeted image-wise distribution.

6. Limitations

While our solution improves the pose annotations, the resulting pose distribution depends on some parameters (tolerance factors, sampling of the SE(3) space, etc.). We selected their values carefully. We invite the reader to check the visualizations in the supplementary material.

Our annotation method relies on a geometric analysis of the scene. It is possible that the sensor resolution, sensor noise, field of view, or motion blur may also affect the visibility of the disambiguating parts. Considering these effects would improve the ground truth even further.

Methods		Train	PMSD	RMSD	PMPD	RMPD
T-LESS [13] Complete dataset						
Distrib	SpyroPose [9]	PBR	32.8	48.1	55.9	55.5
	LiePose-Diffusion [19]	PBR	24.6	71.4	61.2	89.5
	LiePose-Diffusion [19]	PBR + real	29.9	75.4	68.4	90.6
Single	leroy-fuscocclu-rgb	PBR + real	55.4	35.7	80.9	54.2
	gdmppdet-phrealgenflow-multihypo-rgb [28, 44]	PBR + real	52.4	34.9	77.7	52.2
	cosypose-ccv20-syntreal-8views [23]	PBR + real	43.5	25.7	53.1	30.9
T-LESS [13] Only symmetrical objects						
Distrib	SpyroPose [9]	PBR	31.5	42.7	70.5	60.8
	LiePose-Diffusion [19]	PBR	18.3	61.6	63.6	87.3
	LiePose-Diffusion [19]	PBR + real	24.1	67.0	70.3	88.1
Single	leroy-fuscocclu-rgb	PBR + real	52.4	25.7	86.1	45.3
	gdmppdet-phrealgenflow-multihypo-rgb [28, 44]	PBR + real	45.8	20.8	76.5	37.8
	cosypose-ccv20-syntreal-8views [23]	PBR + real	29.1	6.5	40.0	10.5

Table 2. **Comparison of pose distribution estimation methods on T-LESS using our ground truth pose distributions.**

7. Conclusion

For simplicity, most of the 6D pose estimation benchmarks rely on a single 6D pose annotation per image, completed by a per-object symmetry pattern to transform this unique pose into a distribution. We argued that ignoring the per-image nature of the symmetry pattern is prone to bias in the resulting distribution ground truth and in the resulting performances evaluations.

We then proposed a method to annotate 6D pose distribution with a per-image analysis of the object symmetries. We illustrated that the resulting ground truth is more accurate. Moreover, when using this ground truth to re-evaluate current state-of-the-art methods, we showed that the ranking of these methods changes drastically. We also introduced metrics to evaluate methods that estimate a pose distribution and provided their first evaluation on real data.

We believe that these results should encourage the 3D vision community to adopt a new outlook on these methods and how well they work in practice, and should guide future research. To facilitate development, we will make our annotations and code publicly available.

References

- [1] Eric Brachmann, Alexander Krull, Frank Michel, Stefan Gumhold, Jamie Shotton, and Carsten Rother. Learning 6D Object Pose Estimation Using 3D Object Coordinates. In *European Conference on Computer Vision*, 2014. 2
- [2] Romain Brégier, Frédéric Devernay, Laetitia Leyrit, and James L. Crowley. Symmetry-Aware Evaluation of 3D Object Detection and Pose Estimation in Scenes of Many Parts in Bulk. In *International Conference on Computer Vision Workshop*, 2017. 2
- [3] Dingding Cai, Janne Heikkilä, and Esa Rahtu. Sc6D: Symmetry-Agnostic and Correspondence-Free 6D Object Pose Estimation. In *International Conference on 3D Vision*, 2022. 7
- [4] Jianqiu Chen, Zikun Zhou, Mingshan Sun, Rui Zhao, Liwei Wu, Tianpeng Bao, and Zhenyu He. Zeropose: Cad-prompted zero-shot object 6d pose estimation in cluttered scenes. *IEEE Transactions on Circuits and Systems for Video Technology*, 2024. 7
- [5] Andreas Drounoglou, Rigas Kouskouridas, Sotiris Malasiotis, and Tae-Kyun Kim. Recovering 6D Object Pose and Predicting Next-Best-View in the Crowd. In *Conference on Computer Vision and Pattern Recognition*, 2016. 2, 5
- [6] Bertram Drost, Markus Ulrich, Nassir Navab, and Slobodan Ilic. Model Globally, Match Locally: Efficient and Robust 3D Object Recognition. In *Conference on Computer Vision and Pattern Recognition*, 2010. 2
- [7] Bertram Drost, Markus Ulrich, P. Bergmann, P. Härtinger, and Carsten Steger. Introducing MVTEC ITODD - A Dataset for 3D Object Recognition in Industry. In *International Conference on Computer Vision Workshop*, 2017. 2, 5
- [8] Rasmus Laurvig Haugaard and Anders Glent Buch. SurfEmb: Dense and Continuous Correspondence Distributions for Object Pose Estimation with Learnt Surface Embeddings. In *Conference on Computer Vision and Pattern Recognition*, 2022. 2, 6, 7
- [9] Rasmus Laurvig Haugaard, Frederik Hagelskjær, and Thorbjørn Mosekjær Iversen. SpyroPose: SE(3) Pyramids for Object Pose Distribution Estimation. In *International Conference on Computer Vision*, 2023. 1, 2, 3, 5, 6, 7, 8, 9
- [10] Stefan Hinterstoisser, Stefan Holzer, Cédric Cagniard, Slobodan Ilic, Kurt Konolige, Nassir Navab, and Vincent Lepetit. Multimodal Templates for Real-Time Detection of Texture-Less Objects in Heavily Cluttered Scenes. In *International Conference on Computer Vision*, 2011. 2
- [11] Stefan Hinterstoisser, Vincent Lepetit, Slobodan Ilic, Stefan Holzer, Gary Bradski, Kurt Konolige, and Nassir Navab. Model-Based Training, Detection and Pose Estimation of Texture-Less 3D Objects in Heavily Cluttered Scenes. In *Asian Conference on Computer Vision*, 2013. 2
- [12] Tomáš Hodaň, Jiří Matas, and Štěpán Obdržálek. On Evaluation of 6D Object Pose Estimation. In *European Conference on Computer Vision Workshop*, 2016. 3, 4
- [13] Tomáš Hodaň, Pavel Haluza, Štěpán Obdržálek, Jiří Matas, Manolis Lourakis, and Xenophon Zabulis. T-LESS: An RGB-D Dataset for 6D Pose Estimation of Texture-less Objects. In *IEEE Winter Conference on Applications of Computer Vision*, 2017. 1, 2, 6, 7, 8
- [14] Tomáš Hodaň, Frank Michel, Eric Brachmann, Wadim Kehl, Anders Glent Buch, Dirk Kraft, Bertram Drost, Joel Vidal, Stephan Ihrke, Xenophon Zabulis, Caner Sahin, Fabian Manhardt, Federico Tombari, Tae-Kyun Kim, Jiří Matas, and Carsten Rother. BOP: Benchmark for 6D Object Pose Estimation. In *European Conference on Computer Vision Workshop*, 2018. 2, 3
- [15] Tomáš Hodan, Dániel Baráth, and Jiri Matas. EPOS: Estimating 6D Pose of Objects with Symmetries. In *Conference on Computer Vision and Pattern Recognition*, 2020. 2
- [16] Tomáš Hodaň, Martin Sundermeyer, Bertram Drost, Yann Labbé, Eric Brachmann, Frank Michel, Carsten Rother, and Jiří Matas. BOP Challenge 2020 on 6D Object Localization. In *European Conference on Computer Vision Workshop*, 2020. 2, 3
- [17] Tomas Hodan, Martin Sundermeyer, Yann Labbe, Van Nguyen Nguyen, Gu Wang, Eric Brachmann, Bertram Drost, Vincent Lepetit, Carsten Rother, and Jiri Matas. BOP Challenge 2023 on Detection Segmentation and Pose Estimation of Seen and Unseen Rigid Objects. In *IEEE Conf. Comput. Vis. Pattern Recog. Worksh.*, 2024. 1, 5, 6, 7
- [18] Timon Höfer, Benjamin Kiefer, Martin Messmer, and Andreas Zell. Hyperposepdf - Hypernetworks Predicting the Probability Distribution on SO(3). In *Proceedings of the IEEE*, 2023. 2, 3, 8
- [19] Tsu-Ching Hsiao, Hao-Wei Chen, Hsuan-Kung Yang, and Chun-Yi Lee. Confronting Ambiguity in 6D Object Pose Estimation via Score-Based Diffusion on SE(3). In *Conference on Computer Vision and Pattern Recognition*, 2024. 1, 2, 3, 5, 6, 7, 8, 9
- [20] Thorbjørn Mosekjær Iversen, Rasmus Laurvig Haugaard, and Anders Glent Buch. Ki-Pode: Keypoint-Based Implicit Pose Distribution Estimation of Rigid Objects. In *British Machine Vision Conference*, 2022. 3, 5
- [21] Roman Kaskman, Sergey Zakharov, Ivan Shugurov, and Slobodan Ilic. HomebrewedDB: RGB-D Dataset for 6D Pose Estimation of 3D Objects. In *International Conference on Computer Vision Workshop*, 2019. 5
- [22] David Klee, Ondrej Biza, Robert Platt, and Robin Walters. Image to Sphere: Learning Equivariant Features for Efficient Pose Prediction. In *International Conference on Learning Representations*, 2022. 2
- [23] Yann Labbé, Justin Carpentier, Mathieu Aubry, and Josef Sivic. CosyPose: Consistent Multi-View Multi-Object 6D Pose Estimation. In *European Conference on Computer Vision*, 2020. 2, 7, 8
- [24] Yann Labbé, Lucas Manuelli, Arsalan Mousavian, Stephen Tyree, Stan Birchfield, Jonathan Tremblay, Justin Carpentier, Mathieu Aubry, Dieter Fox, and Josef Sivic. MegaPose: 6D Pose Estimation of Novel Objects via Render & Compare. In *Proceedings of the 6th Conference on Robot Learning (CoRL)*, 2022. 7
- [25] Yuelong Li, Yafei Mao, Raja Bala, and Sunil Hadap. Mrcnet: 6-dof pose estimation with multiscale residual correla-

- tion. In *Proceedings of the IEEE/CVF Conference on Computer Vision and Pattern Recognition*, 2024. 7
- [26] Jiehong Lin, Lihua Liu, Dekun Lu, and Kui Jia. SAM-6D: Segment Anything Model Meets Zero-Shot 6D Object Pose Estimation. In *Conference on Computer Vision and Pattern Recognition*, 2024. 7
- [27] Yongliang Lin, Yongzhi Su, Praveen Nathan, Sandeep Inuganti, Yan Di, Martin Sundermeyer, Fabian Manhardt, Didier Stricker, Jason Rambach, and Yu Zhang. Hipose: Hierarchical Binary Surface Encoding and Correspondence Pruning for RGB-D 6Dof Object Pose Estimation. In *Conference on Computer Vision and Pattern Recognition*, 2024. 7
- [28] Xingyu Liu, Ruida Zhang, Chenyangguang Zhang, Bowen Fu, Jiwen Tanq, Xiquan Lianq, Jinqyo Tanq, Xiaotian Chenq, Yukang Zhanq, Gu Wang, and Xiangyang Ji. Gdrnp. In *a submission to the BOP Challenge 2022. Unpublished*, 2022. 7, 8
- [29] Fabian Manhardt, Diego Martin Arroyo, Christian Rupprecht, Benjamin Busam, Tolga Birdal, Nassir Navab, and Federico Tombari. Explaining the Ambiguity of Object Detection and 6D Pose from Visual Data. In *International Conference on Computer Vision*, 2019. 1, 2
- [30] Fabrice Mayran de Chamisso, Boris Meden, and Mohamed Tamaazousti. HSPA: Hough Space Pattern Analysis as an Answer to Local Description Ambiguities for 3D Pose Estimation. In *British Machine Vision Conference*, 2022. 2
- [31] Boris Meden, Pablo Vega, Mayran De Chamisso, Fabrice, and Steve Bourgeois. Introducing CEA IMSOLD - A Dataset for Multi-Scale Object Localization in Industry. In *International Conference on Robotics and Automation*, 2024. 2
- [32] Sungphill Moon, Hyeontae Son, Dongcheol Hur, and Sangwook Kim. Genflow: Generalizable Recurrent Flow for 6D Pose Refinement of Novel Objects. In *Conference on Computer Vision and Pattern Recognition*, 2024. 7
- [33] Kieran A. Murphy, Carlos Esteves, Varun Jampani, Srikumar Ramalingam, and Ameesh Makadia. Implicit-PDF: Non-Parametric Representation of Probability Distributions on the Rotation Manifold. In *International Conference on Machine Learning*, 2021. 2, 3, 5, 8
- [34] Van Nguyen Nguyen, Thibault Groueix, Georgy Ponimatkin, Vincent Lepetit, and Tomas Hodan. CNOS: A Strong Baseline for CAD-Based Novel Object Segmentation. In *International Conference on Computer Vision Workshop*, 2023. 7
- [35] Van Nguyen Nguyen, Thibault Groueix, Mathieu Salzmann, and Vincent Lepetit. GigaPose: Fast and Robust Novel Object Pose Estimation via One Correspondence. In *Conference on Computer Vision and Pattern Recognition*, 2024. 7
- [36] Brian Okorn, Mengyun Xu, Martial Hebert, and David Held. Learning Orientation Distributions for Object Pose Estimation. In *International Conference on Intelligent Robots and Systems*, 2020. 2
- [37] Evin Pınar ÖRnek, Yann Labbé, Bugra Tekin, Lingni Ma, Cem Keskin, Christian Forster, and Tomas Hodan. Foundpose: Unseen Object Pose Estimation with Foundation Features. In *arXiv Preprint*, 2023. 7
- [38] Kiru Park, Timothy Patten, and Markus Vincze. Pix2Pose: Pixel-Wise Coordinate Regression of Objects for 6D Pose Estimation. In *International Conference on Computer Vision*, 2019. 2
- [39] Arul Selvam Periyasamy, Luis Denninger, and Sven Behnke. Learning Implicit Probability Distribution Functions for Symmetric Orientation Estimation from RGB Images Without Pose Labels. In *International Conference on Robotic Computing*, 2022. 3
- [40] Yongzhi Su, Mahdi Saleh, Torben Fetzner, Jason Rambach, Nassir Navab, Benjamin Busam, Didier Stricker, and Federico Tombari. Zebrapose: Coarse to Fine Surface Encoding for 6Dof Object Pose Estimation. In *Conference on Computer Vision and Pattern Recognition*, 2022. 2, 7
- [41] Martin Sundermeyer, Zoltan-Csaba Marton, Maximilian Durner, and Rudolph Triebel. Augmented Autoencoders: Implicit 3D Orientation Learning for 6D Object Detection. *International Journal of Computer Vision*, 128, 2020. 2
- [42] Martin Sundermeyer, Tomáš Hodaň, Yann Labbe, Gu Wang, Eric Brachmann, Bertram Drost, Carsten Rother, and Jiří Matas. Bop Challenge 2022 on Detection, Segmentation and Pose Estimation of Specific Rigid Objects. In *Conference on Computer Vision and Pattern Recognition*, 2023. 2, 5, 7, 1
- [43] Stephen Tyree, Jonathan Tremblay, Thang To, Jia Cheng, Terry Mosier, Jeffrey Smith, and Stan Birchfield. 6-DoF Pose Estimation of Household Objects for Robotic Manipulation: An Accessible Dataset and Benchmark. In *International Conference on Intelligent Robots and Systems*, 2022. 2, 3, 5
- [44] Gu Wang, Fabian Manhardt, Federico Tombari, and Xiangyang Ji. GDR-Net: Geometry-guided Direct Regression Network for Monocular 6D Object Pose Estimation. In *Conference on Computer Vision and Pattern Recognition*, 2021. 2, 7, 8
- [45] Pengyuan Wang, HyunJun Jung, Yitong Li, Siyuan Shen, Rahul Parthasarathy Srikanth, Lorenzo Garattoni, Sven Meier, Nassir Navab, and Benjamin Busam. PhoCaL: A Multi-Modal Dataset for Category-Level Object Pose Estimation with Photometrically Challenging Objects. In *Conference on Computer Vision and Pattern Recognition*, 2022. 2
- [46] Bowen Wen, Wei Yang, Jan Kautz, and Stan Birchfield. Foundationpose: Unified 6D Pose Estimation and Tracking of Novel Objects. In *Conference on Computer Vision and Pattern Recognition*, 2024. 7
- [47] Yu Xiang, Tanner Schmidt, Venkatraman Narayanan, and Dieter Fox. PoseCNN: A Convolutional Neural Network for 6D Object Pose Estimation in Cluttered Scenes, 2018. 2, 3, 6, 7
- [48] Ruida Zhang, Ziqin Huang, Gu Wang, Xingyu Liu, Chenyangguang Zhang, and Xiangyang Ji. GPose2023. In *a submission to the BOP Challenge 2023. Unpublished*, 2023. 7, 10

BOP-Distrib: Revisiting 6D Pose Estimation Benchmarks for Better Evaluation under Visual Ambiguities

Supplementary Material

1. Analysis of our BOP-D Annotations

1.1. Additional BOP-D Ground Truths Visualizations

We first provide more visualizations for qualitative appreciation of the new ground truth annotations accuracy in Figure 5.

These images are taken from a video compilation of all ground truth annotations sorted by object identifier, also provided as supplementary material ([BOP_D_id239_supp_newGT_visualizations.mp4](#)), to convince the reader of their quality. We invite the reader to stop on some frames and check that the distribution recovered by our method does correspond to the ambiguities in the image for the object in the bounding box.

1.2. Differences between Original Annotations and Ours

Figure 4 visualizes the differences between the poses that are accepted by BOP and the ones accepted when using our annotations. For this purpose, for each object, we provide a bar plot. This bar plot shows, for each image where the object appears, the percentage of poses considered correct by BOP that are also considered correct with our annotations. The bar plots show the percentages after sorting them, i.e., the bar on the left corresponds to the image with the smallest difference.

The annotations for some objects remain mostly unchanged. But because our method analyses more finely the possible object symmetries, many poses are actually not accepted with our annotations for the other objects.

2. Computing the Pose Estimation Results

2.1. T-LESS Pose Estimation and Unseen Objects Pose Estimation

Recently, the BOP challenge [42] made public the pose estimations results of the methods evaluated in the leaderboard³. Based on these results and the BOP toolkit⁴ in which we implemented the variations of **MSSD** and **MSPD**, that use our per-image symmetries patterns instead of BOP global object symmetries, we were able to reprocess these pose estimates against our new ground truths. Our results have been presented in Table 1. Section 3 of supplementary

³<https://bop.felk.cvut.cz/leaderboards/>

⁴https://github.com/thodan/bop_toolkit/tree/master

material illustrates some of the failure cases with the new and more accurate ground truth.

2.2. Computation of the SpyroPose [9] Distribution Results

The implementation provided by the authors of SpyroPose allows to train a network for one object of T-LESS. We batched the training stage for all objects, and then batched the inference. For one object, SpyroPose produces more than 100 000 estimates, sorted by their probabilities, as it samples $SO(3) \times \mathbb{R}^3$ (using a slice of \mathbb{R}^3). As the probabilities of these estimates quickly tend to zero, we reduce their distributions to the 400 best estimates. These 400 estimates are used for the evaluations of Section 5.4.

As no pose distribution evaluation existed, the authors of [9] reported only per-object averaged log-likelihood against BOP original ground truth.

2.3. Computation of the Lie-Pose Diffusion [19] Distribution Results

The implementation provided by the authors of Lie-Pose allows to train a network for all objects of T-LESS. The inference phase produces one pose estimate per image crop. We batched the inference phase, with varying seeds. We then merged all these estimates into a single set of poses per image crop. The authors report 1000 runs to produce a distribution. For our evaluation, we ran the code 100 times with different noises to produce Lie-Pose distribution results.

As no pose distribution evaluation existed, the authors of [19] reported only few illustrations of pose distributions results on T-LESS. They evaluated their method as a single pose estimation method, with a single run of the method.

3. Illustrations of Single Pose Re-evaluation

We provide here more cues about the changes in the Single Pose ranking, based on the **MSSD** and **MSPD** metrics using our new more accurate ground truth.

To do so, we look at the pose estimates of the method GDRNPP v1.4. When we evaluated GDRNPP v1.4 estimates against our new ground truths, it changed the method ranking from rank 6 to rank 10 in Table 1. Even more interestingly, the metrics went down from an **MSSD** of 88.4 and an **MSPD** of 90.9 to an **MSSD** of 60.6 and an **MSPD** of 63.7.

Figure 6 illustrates why **MSSD** and **MSPD** changed for this method. It appears that, although GDRNPP v1.4 estimates were close to the ground truth pose, its rotations were

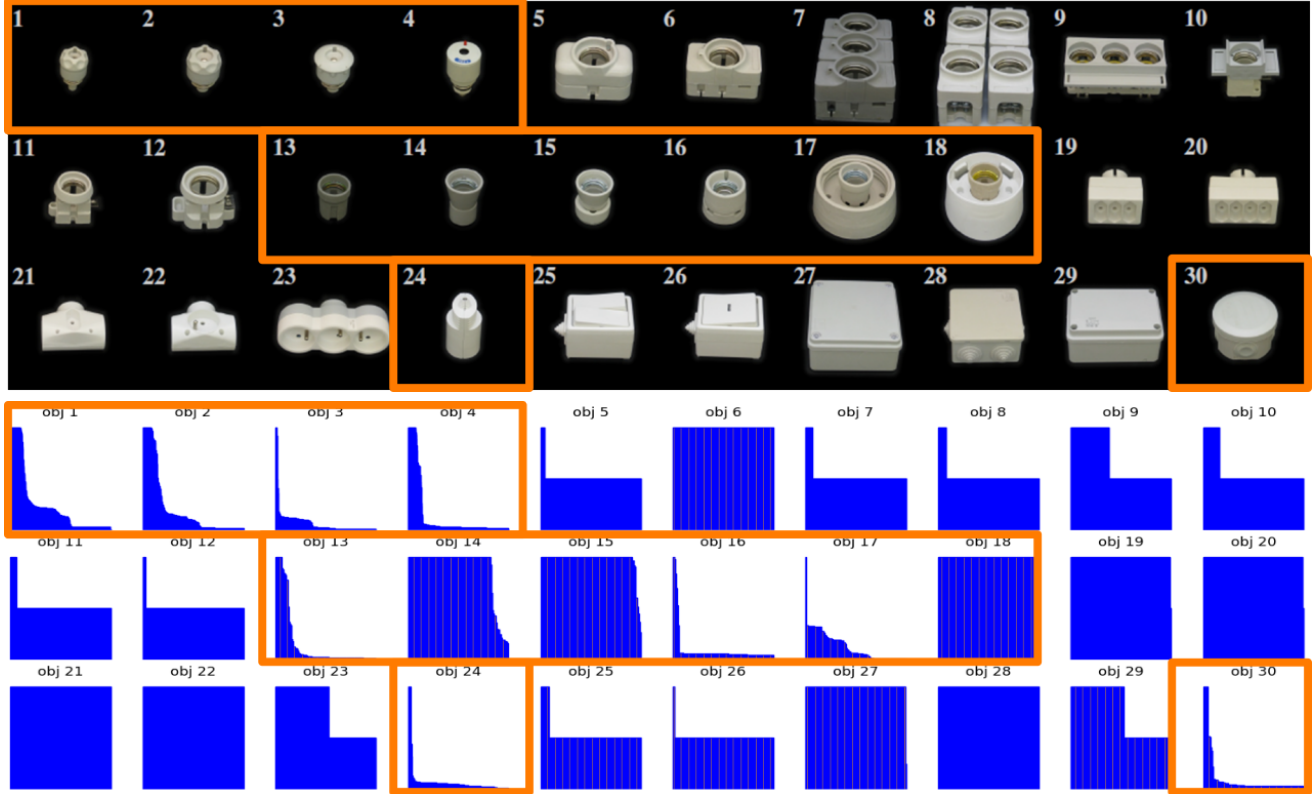


Figure 4. **Visualization of annotation changes compared to the T-LESS original annotations.** **Top:** T-LESS objects with their identifier. **Bottom:** For each object, we plot the percentages of poses kept from the original annotations by our method over the images (sorted by percentages). T-LESS assumes full rotational symmetries, while our annotation method captures more complex symmetry patterns. Only Object 18 is perfectly symmetrical and our method retrieves the same poses as the original annotations. For the other objects, in particular the objects with complex symmetry patterns like the first 4 objects. Our annotations significantly change the original annotations. The objects annotated as 'circular' in BOP are highlighted in orange.

not precise. When they are evaluated against a symmetries pattern that is not precise, the evaluation appears correct. Our new ground truth shows that GDRNPP v1.4 tends not to align correctly some of the objects. Hence the drop in performances.

4. Visualizing results by SpyroPose [9]

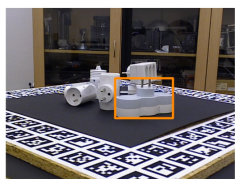
We display some of SpyroPose distribution estimates against our ground truth in Figure 7. For the case of the three instances of Object 1, SpyroPose correctly retrieves the single mode for Instance 1. The continuous symmetry of Instance 2 is partially retrieved.

5. Visualizing results by LiePose diffusion [19]

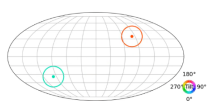
We show some of LiePose [19] distribution estimates against our ground truth in Figure 8. Similarly to SpyroPose [9], LiePose [19] is able to retrieve the single mode of Instance 1, but gets better results when estimating continuous distributions.

Figures 9, 10, 11 and 12 compare SpyroPose [9] and LiePose [19] results on objects with discrete and continuous symmetries. SpyroPose [9] rotations tends to be more precise than LiePose [19], but misses some of the modes. LiePose [19] tends to estimate continuous symmetries when the image produces discrete ones. These images are taken from a video compilation of SpyroPose [9] and LiePose [19] results also provided as supplementary material ([BOP_D_id239_supp_distribution_comparison_SpyroPose_LiePose.mp4](#)). Scenes with single instance of objects have been chosen, to facilitate visualization. We invite the reader to stop on some frames and check the differences in the estimates. Our ground truth distribution is displayed as the envelop for the rotation part and as red stars for the translation part.

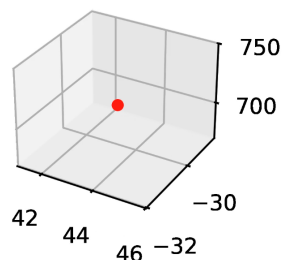
Object 23, Scene 8, Image 441



Input image with target object in bounding box



Recovered distribution rotation part

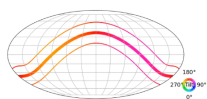


Recovered distribution translation part

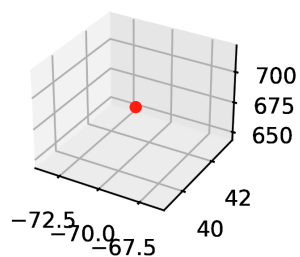
Object 15, Scene 16, Image 194



Input image with target object in bounding box



Recovered distribution rotation part

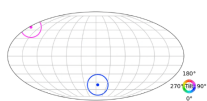


Recovered distribution translation part

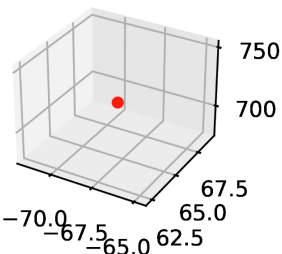
Object 19, Scene 13, Image 144



Input image with target object in bounding box



Recovered distribution rotation part

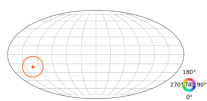


Recovered distribution translation part

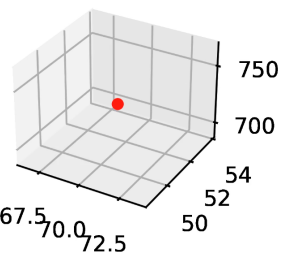
Object 7, Scene 17, Image 121



Input image with target object in bounding box

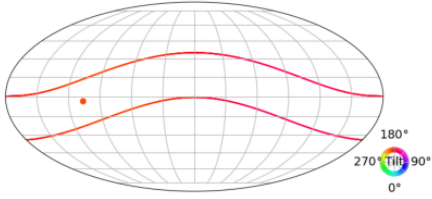


Recovered distribution rotation part

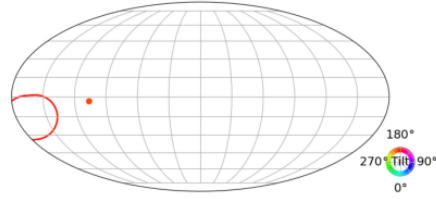


Recovered distribution translation part

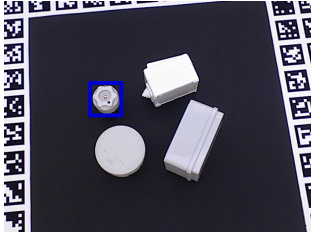
Figure 5. **Visualizing some BOP-D ground truths as computed by our method.** Each example features an object of interest, in the bounding box in the left image, and its BOP-D pose distribution, split between the rotation part (center) and translation part (right). As no object present symmetries in translation here, the translation part of the distribution is always on the same point of \mathbb{R}^3 . We provide much more examples in the accompanying video.



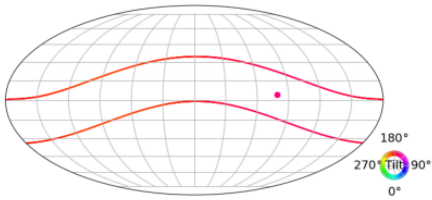
(a) BOP continuous symmetry pattern of Object 2 (envelop) and GDRNPP v1.4 estimate (plain circle). The circle belongs to the envelop, yielding a low **MSSD** error of 4.46.



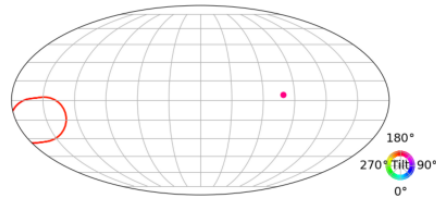
(b) Our visual symmetry pattern (the much smaller envelop) and GDRNPP estimate (plain circle). The circle does not belong to the envelop anymore, the **MSSD** error becomes 21.62.



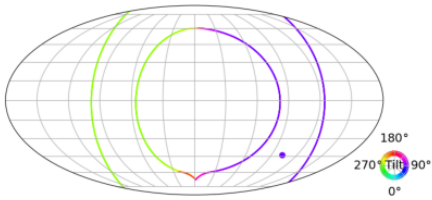
(c) Corresponding image for (a) and (b): T-LESS Scene 1, Image 17, Object 2 (in bounding box).



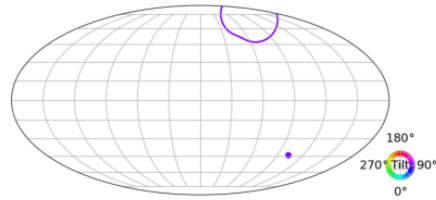
(d) BOP continuous symmetry pattern for Object 1 (envelop) and GDRNPP v1.4 estimate (plain circle). The circle belongs to the envelop, yielding a low **MSSD** error of 9.43.



(e) Our visual symmetry pattern (much smaller envelop) and GDRNPP estimate (plain circle). The circle does not belong to the envelop anymore, the **MSSD** error becomes 32.87.



(f) BOP continuous symmetry pattern of Object 4 (envelop) and GDRNPP v1.4 estimate (plain circle). The circle belongs to the envelop, yielding a low **MSSD** error of 3.33.



(g) Our visual symmetry pattern (much smaller envelop) and GDRNPP estimate (plain circle). The circle does not belong to the envelop anymore, the **MSSD** error becomes 35.38.



(h) Corresponding image for T-LESS Scene 5, Image 70, Objects 1 (d-e) and 4 (f-g), in bounding boxes).

Figure 6. **Impact of our annotations on Single Pose evaluation.** We show here cases where the estimates by a state-of-the-art method (GDRNPP v1.4) produces fairly good **MSSD** errors when considering ground truth provided by BOP. For these cases, our more accurate ground truth yields worse **MSSD** errors, as it appears that the estimate belongs to the global symmetry pattern, but does not explain what is visible in the image.

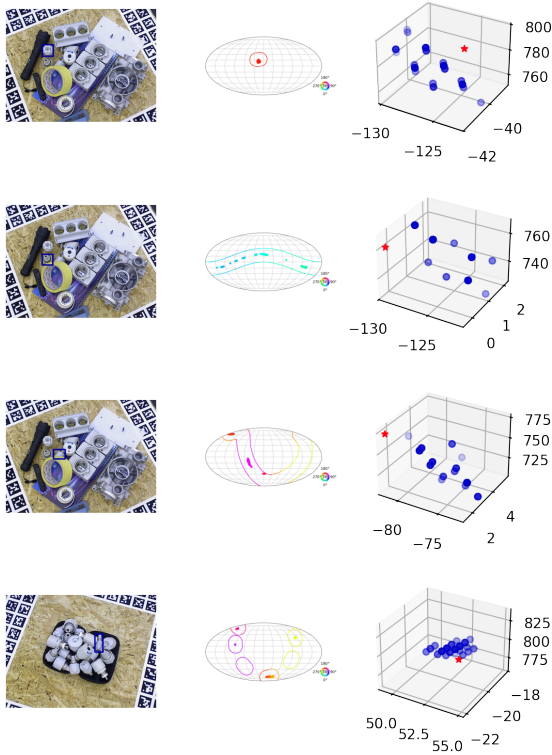


Figure 7. **Illustration of SpyroPose [9] results.** We show the distribution estimates for the 3 instances of Object 1 (in the bounding box). The ground truth distribution is displayed as an envelop for the rotation part and as red star for the translation part.

6. Using Our Per-Image Annotations for Other Pose Estimation Datasets

Among BOP datasets, ITODD [7] and Home-BrewedDB [21] are the two other presenting object symmetries. They could easily be processed by our method, however their ground truth poses, needed as input to our method, are not public.

We give here an illustration of the interest to reprocess their symmetries patterns. We take ITODD’s small validation set, for which the ground truth is public. Figure 13 presents our result for the star object new ground truth, as well as one case of the current best performer (gpose2023) failing to align the holes. In the current version of BOP evaluation, this pose estimation is validated. With our annotations, it would be penalized.

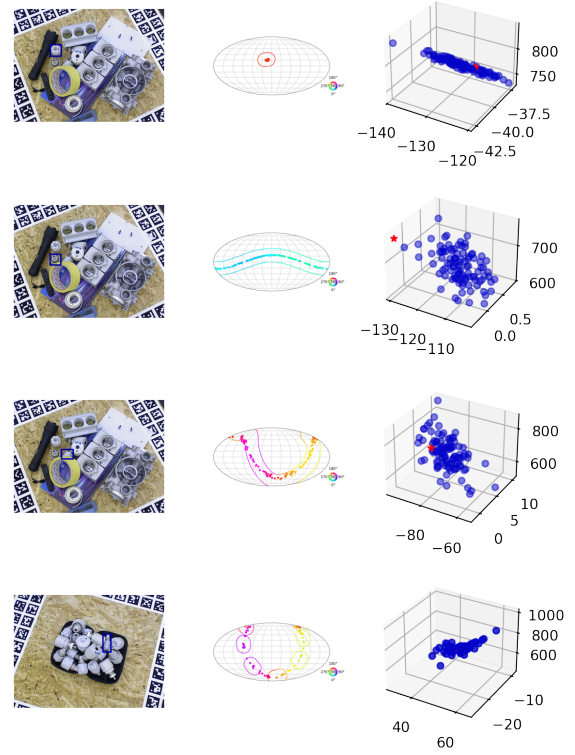


Figure 8. **Illustration of LiePose [19] results.** We show the distribution estimates for the 3 instances of Object 1 (in the bounding box). The ground truth distribution is displayed as an envelop for the rotation part and as red star for the translation part.

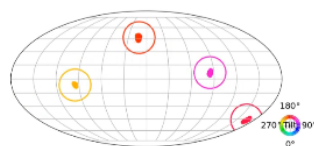
Acknowledgment

The authors thank Rasmus Laurvig Haugaard for providing SpyroPose [9] implementation for baseline evaluation.

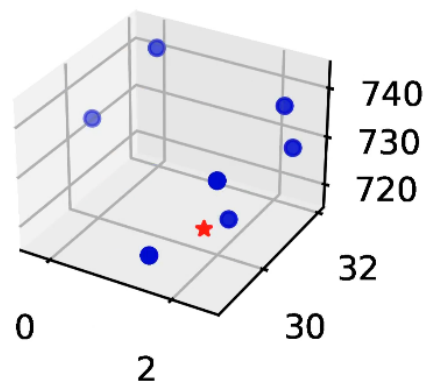
Object 27, Scene 5, Image 221



Input image with target object in bounding box



SpyroPose[7] distribution rotation part

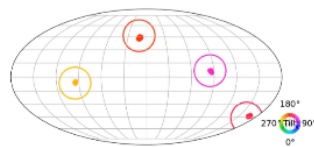


SpyroPose[7] distribution translation part

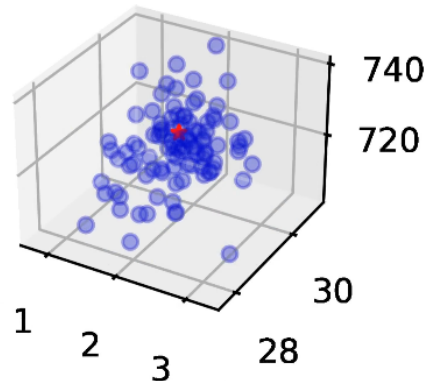
Object 27, Scene 5, Image 221



Input image with target object in bounding box



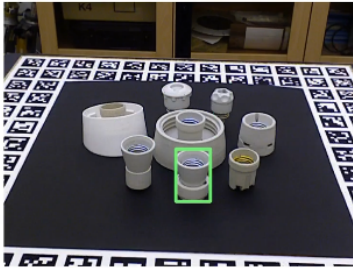
LiePose[17] distribution rotation part



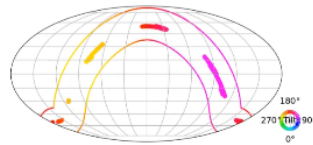
LiePose[17] distribution translation part

Figure 9. Visualizing SpyroPose [9] (top row) and LiePose [19] (bottom row) distribution results for object 27 (four rotation modes). Each example features an object of interest, in the bounding box in the left image, and the methods distribution estimation, split between the rotation part (center) and translation part (right). Both methods are able to retrieve the four rotation modes of the object. The envelop in the rotation part represents our BOP-D annotation. We provide much more examples in the accompanying video.

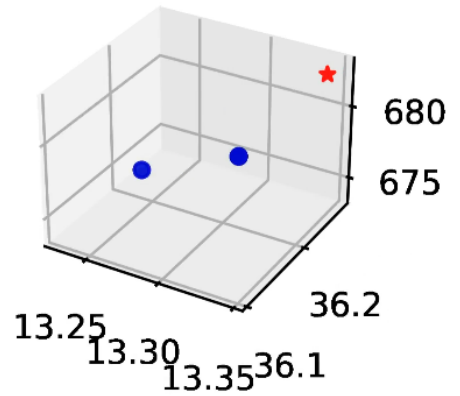
Object 15, Scene 7, Image 342



Input image with target object in bounding box

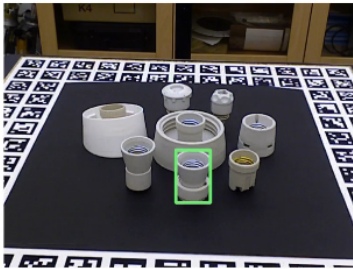


SpyroPose[7] distribution rotation part

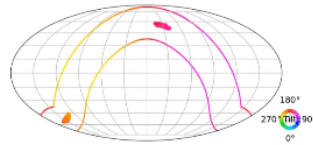


SpyroPose[7] distribution translation part

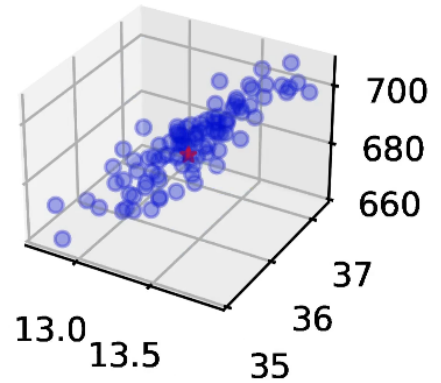
Object 15, Scene 7, Image 342



Input image with target object in bounding box



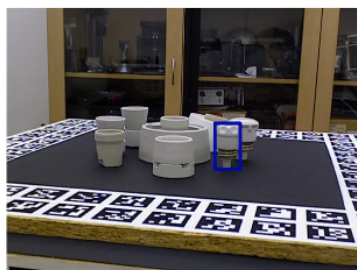
LiePose[17] distribution rotation part



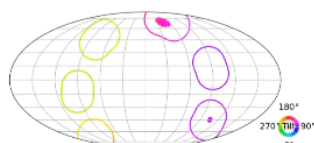
LiePose[17] distribution translation part

Figure 10. Visualizing SpyroPose [9] (top row) and LiePose [19] (bottom row) distribution results for object 15 (continuous rotation). Each example features an object of interest, in the bounding box in the left image, and the methods distribution estimation, split between the rotation part (center) and translation part (right). Both methods fail to generate the target continuous rotation, although SpyroPose produces more correct rotations. The envelop in the rotation part represents our BOP-D annotation. We provide much more examples in the accompanying video.

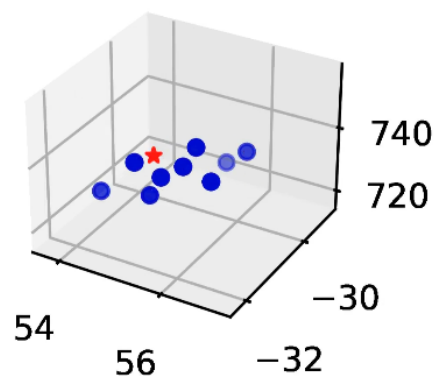
Object 1, Scene 7, Image 435



Input image with target object in bounding box

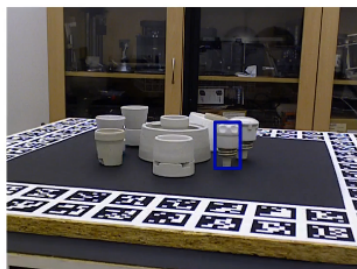


SpyroPose[7] distribution rotation part

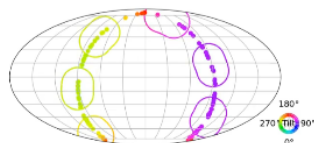


SpyroPose[7] distribution translation part

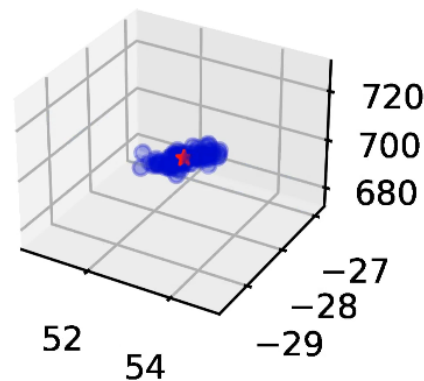
Object 1, Scene 7, Image 435



Input image with target object in bounding box



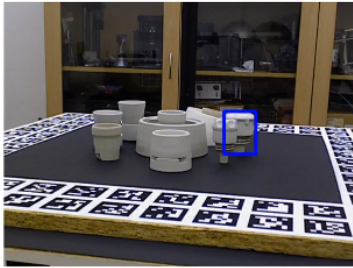
LiePose[17] distribution rotation part



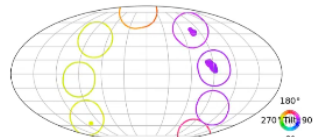
LiePose[17] distribution translation part

Figure 11. Visualizing SpyroPose [9] (top row) and LiePose [19] (bottom row) distribution results for object 1 (six rotation modes). Each example features an object of interest, in the bounding box in the left image, and the methods distribution estimation, split between the rotation part (center) and translation part (right). For this case of six rotations modes, SpyroPose is able to retrieve only two of them, whereas LiePose tends to a continuous distribution, thus generating false rotations. The envelop in the rotation part represents our BOP-D annotation. We provide much more examples in the accompanying video.

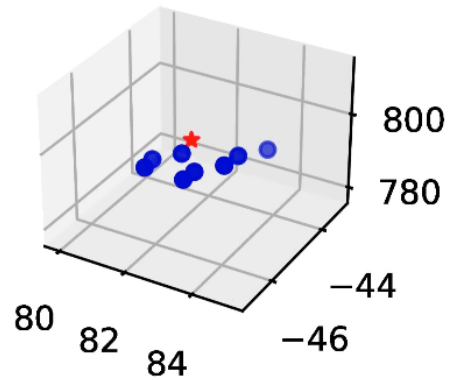
Object 3, Scene 7, Image 435



Input image with target object in bounding box

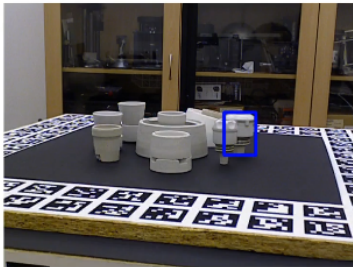


SpyroPose[7] distribution rotation part

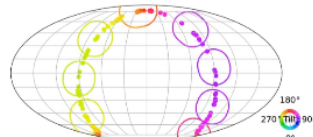


SpyroPose[7] distribution translation part

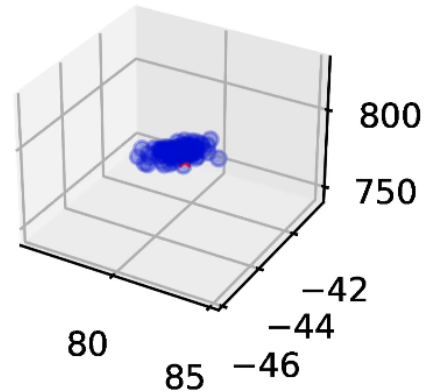
Object 3, Scene 7, Image 435



Input image with target object in bounding box



LiePose[17] distribution rotation part



LiePose[17] distribution translation part

Figure 12. Visualizing SpyroPose [9] (top row) and LiePose [19] (bottom row) distribution results for object 3 (eight rotation modes). Each example features an object of interest, in the bounding box in the left image, and the methods distribution estimation, split between the rotation part (center) and translation part (right). For this case of eight rotations modes, SpyroPose is able to retrieve only two of them, whereas LiePose tends to a continuous distribution, thus generating false rotations. The envelop in the rotation part represents our BOP-D annotation. We provide much more examples in the accompanying video.

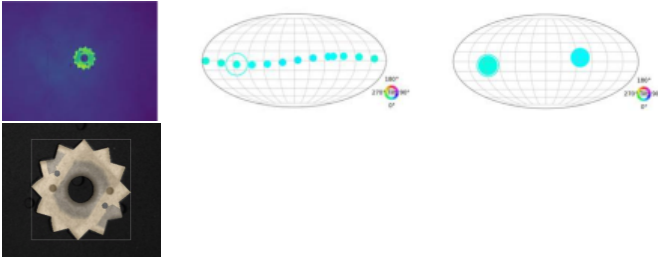


Figure 13. **Illustration of ITODD symmetries on the validation set (with public GT).** For the star image (left, first row), BOP symmetries display 12 rotation modes (middle), whereas our method would keep only 2 rotation modes, which align the two holes (right) (size was set to one over the number of modes, hence the bigger modes on the right). We also show a pose estimate of GPose [48], ranked first at BOP 2023, for the star object overlaid on its image. We observe that the holes are not correctly aligned. **MSPD** and **MSSD** metrics validate this estimate, whereas **MSPD** and **MSSD** metrics with our new annotations would have penalized it.